






Quantum Cascade Surface Emitting Lasers

Journal Article

Author(s):

[Stark, David](#) ; [Kapsalidis, Filippos](#) ; [Markmann, Sergej](#); [Bertrand, Mathieu](#) ; [Marzban, Bahareh](#); [Gini, Emilio](#); [Beck, Mattias](#) ; [Faist, Jérôme](#) 

Publication date:

2024-08

Permanent link:

<https://doi.org/10.3929/ethz-b-000668690>

Rights / license:

[Creative Commons Attribution 4.0 International](#)

Originally published in:

Laser & Photonics Reviews 18(8), <https://doi.org/10.1002/lpor.202300663>

Quantum Cascade Surface Emitting Lasers

David Stark,* Filippos Kapsalidis, Sergej Markmann, Mathieu Bertrand, Bahareh Marzban, Emilio Gini, Mattias Beck, and Jérôme Faist*

A low-cost single frequency laser, emitting in the mid-infrared spectral region and dissipating minimal electrical power, is a key ingredient for the next generation of portable gas sensors for high-volume applications involving chemical sensing of important greenhouse and pollutant gases. Herein, a Quantum Cascade Surface Emitting Laser (QCSEL) is proposed, which is implemented as a short linear cavity with high reflectivity coated end-mirrors to suppress any edge emission and employs a buried semiconductor diffraction grating to extract the light from the surface. By wafer-level testing, the cavity length scaling is investigated, mirror reflectivities larger than 0.9 are extracted, and a pulsed threshold power dissipation of 237 mW for an emission wavelength near 7.5 μm is achieved. Finally, single-mode emission with a side-mode suppression ratio larger than 33 dB is demonstrated for a 248 μm short cavity, which is mounted with the epitaxial layer up and operated in continuous wave at 20 $^{\circ}\text{C}$.

The Quantum Cascade Laser (QCL), relying on intersubband transitions, is an excellent candidate for a compact and coherent MIR light source because the emission wavelength can be tailored in wide ranges between 3 and 24 μm , as well as between 60 and 300 μm .^[5] The QCL can be modulated up to tens of GHz^[6] and exhibits narrow linewidths,^[7] making it the source of choice for fast high-resolution gas spectroscopy in the MIR.

However, harnessing intersubband transitions comes at the price of large threshold current densities ($\geq 0.47 \text{ kAcm}^{-2}$),^[8] which leads to an electrical power dissipation of several watts if a large device area is employed, hindering the integration into portable applications. By scaling the cavity length, the electrical power dissipation can be

reduced, provided that low optical losses can be maintained to achieve laser action in continuous wave (CW) above room-temperature. Particularly, high mirror reflectivities, with values close to unity, are essential to mitigate the increase of the mirror losses α_m with the reciprocal cavity length $1/L$. This can be seen by considering the threshold current density J_{th} of a linear cavity given by

$$J_{\text{th}} = \frac{\alpha_i + \alpha_m}{g\Gamma} = \frac{1}{g\Gamma} \left(\alpha_i + \frac{\ln(1/R)}{L} \right) \quad (1)$$

where g is the material gain, Γ the optical confinement factor, α_i the internal losses, and R the mirror reflectivity. Naturally, short cavity lasers not only enable smaller device footprints and thus a higher integration density, but they also offer a reduced number of axial lasing modes within the finite gain bandwidth and hence a route toward single axial mode selection. While the Vertical Cavity Surface Emitting Laser (VCSEL) provides an excellent approach for interband lasers emitting in the near-infrared spectral region,^[9] it has also led to electrically pumped room-temperature demonstrations for short MIR wavelengths.^[10–12] However, this approach is not applicable to QCLs because of the strict intersubband selection rule, which requires the electric field of the optical mode to be perpendicular to the plane of the quantum wells.^[13]

For QCLs, an extensively studied approach is the grating-coupled ring cavity surface emitting QCL.^[14–18] These large-area QCLs feature diameters on the order of 400 μm and the single mode is selected through a resonant second-order grating. Single-mode operation through cavity length scaling has been achieved at cryogenic temperatures with both disk cavity

1. Introduction

The mid-infrared (MIR) spectral region, spanning from 3 to 30 μm , is the molecular “fingerprint” region for many important organic and inorganic molecules, as they exhibit strong and narrow absorption lines within this region.^[1,2] Miniaturized optical gas sensors based on MIR absorption spectroscopy are highly attractive^[3] for many applications such as industrial process control, environmental monitoring, and medical diagnosis.^[4] To enable low-cost and portable MIR gas sensors, compact, and low power dissipation single-mode light sources operating in the range of interest are of uttermost importance.

D. Stark, F. Kapsalidis, S. Markmann, M. Bertrand, B. Marzban, M. Beck, J. Faist

Institute for Quantum Electronics

Department of Physics

ETH Zurich

Zurich 8093, Switzerland

E-mail: starkd@phys.ethz.ch; jfaist@ethz.ch

E. Gini

FIRST Center for Micro- and Nanoscience

ETH Zurich

Zurich 8093, Switzerland

 The ORCID identification number(s) for the author(s) of this article can be found under <https://doi.org/10.1002/lpor.202300663>

© 2024 The Authors. Laser & Photonics Reviews published by Wiley-VCH GmbH. This is an open access article under the terms of the [Creative Commons Attribution](#) License, which permits use, distribution and reproduction in any medium, provided the original work is properly cited.

DOI: 10.1002/lpor.202300663

QCLs^[19,20] and linear ridge QCLs.^[21,22] In the case of linear cavities, lengths of about 100 μm were realized by either using deeply etched Bragg mirrors with reflectivities larger than 0.8,^[21] or by cleaving and depositing highly reflective (HR) metallic coatings with reflectivities of 0.95 and 0.75 on the front and back facet, respectively.^[22]

Superior CW temperature performance can be achieved with buried heterostructure QCLs^[23,24] featuring efficient thermal extraction^[25] and low waveguide losses (0.5 cm^{-1}).^[26] Using a cavity length of 500 μm with a metallic HR coated back facet ($\text{Al}_2\text{O}_3/\text{Ti}/\text{Au}/\text{Al}_2\text{O}_3$) and a partial HR coated front facet ($\text{Al}_2\text{O}_3/\text{Ge}$), threshold dissipation powers of 260 mW at 10 °C and 330 mW at 40 °C have been reported.^[27] Recently, a CW threshold dissipation power of only 143 mW at 20 °C has been demonstrated with a cleaved 250 μm short cavity.^[28] This was achieved by fabricating a subwavelength aperture in the metallic HR coating ($\text{Al}_2\text{O}_3/\text{Au}$) on both facets to suppress diffraction losses.

Those approaches show that metallic HR coatings are effective for shortening the cavity length, although both facets need to be coated, and an aperture is required to still extract light due to the low transmissivity of the metallic layer. To this end, buried second order diffraction gratings^[29,30] open up a way to couple out the light vertically. Furthermore, to scale the cavity length below 200 μm ,^[22] cleaving is not suitable, because the mechanical handling is challenging and the cavity length cannot precisely be controlled. Dry-etching controlled by lithography instead offers a promising alternative.

Therefore, we introduce the Quantum Cascade Surface Emitting Laser (QCSEL), which is essentially an in-plane semiconductor laser implemented in a microcavity, combining an outcoupling element with HR mirrors to suppress any edge emission. Here, we realize the QCSEL as a linear buried heterostructure laser with a buried second order grating in the vicinity of the waveguide, dry-etched facets, and HR coatings deposited on wafer level. We demonstrate the operation of QCSELS with two different active regions designed for 4.5 and 8 μm emission wavelength. We utilize wafer-level testing to investigate the cavity length scaling to assess the mirror reflectivity and to ultimately reduce the power dissipation and the number of lasing modes.

2. Experimental Section

For this work, two strain-balanced InGaAs/AlInAs active regions grown on InP substrates by molecular beam epitaxy (MBE) were used. From electroluminescence measurements, the peak wavelength and the full width half maxima estimating the gain bandwidth were inferred for both active regions. These values, together with the sheet doping densities and the relevant fabrication parameters discussed below, are summarized in **Table 1**.

The buried heterostructure fabrication process^[31,32] started with the definition and wet-etching of the second order grating on the top n-InGaAs cladding layer. The waveguide core was also formed by wet-etching. The lateral semi-insulating InP:Fe blocking layer and the top InP:Si contact layer were regrown by means of metal-organic vapor phase epitaxy (MOVPE). After depositing the metallic top-contact (Ti/Pt/Au), the end-mirror facets were dry-etched with inductively coupled plasma (ICP). Subsequently, both facets were coated with $\text{Si}_3\text{N}_4/\text{Ti}/\text{Au}$ to build HR end-mirrors. The former dielectric layer was deposited by

Table 1. Overview of the fabricated quantum cascade active regions: Peak wavelength λ_0 and full width half maximum 2γ extracted from electroluminescence spectra, nominal sheet doping density n_{2D} , thickness of the top n-InGaAs cladding layer t_{top} , etch depth for the grating d_{etch} , and the thickness of the dielectric coating t_{coat} extracted from scanning electron microscopy (SEM) cross-section images.

Active region	EV1464	EV2616
λ_0 (μm)	4.5	8
2γ (cm^{-1})	238	198
n_{2D} (10^{11}cm^{-2})	1.49	1.04
t_{top} (nm)	200	300
d_{etch} (nm)	95	236
t_{coat} (nm)	435	300

plasma-enhanced chemical vapor deposition (PECVD) and the latter metallic layers by electron beam evaporation. Note that for the metallic coating a Ti adhesion layer before the Au deposition was necessary for further processing and its thickness was estimated to be thinner than 20 nm. After revealing the top-contact by wet- and dry-etching, an additional Au layer with a thickness between 3 to 5 μm was electroplated. Lastly, the substrate was thinned down to about 200 μm and a back contact (Ge/Au/Ni/Au) was deposited. The QCSEL device architecture is illustrated in **Figure 1** with fabrication images and cross-section schematics.

The reflectivity of the HR end-mirrors is estimated by performing 3D simulations (COMSOL) of a 1 μm long waveguide section terminated with a $\text{Si}_3\text{N}_4/\text{Au}$ coating, as illustrated in **Figure 2a**. The modal reflectivities for varying dielectric coating thickness t_{coat} with and without Ti adhesion layer are shown in **Figure 2b**. Modal reflectivities exceeding 0.96 and 0.89 are expected for wavelengths of 4.5 and 8 μm , respectively. At a wavelength of 8 μm , the absorption losses of Si_3N_4 are significant,^[33] and although thinner coatings would be more beneficial, $t_{\text{coat}} = 300\text{ nm}$ was chosen to ensure the electrical insulation of the coating.

In this work, the active device length was scaled from 504 μm down to 46 μm . Approximating the cavity length L by the active device length and neglecting the optical path length in the HR coatings ($L \gg t_{\text{coat}}$), the free spectral range $\Delta\nu$ can be written as

$$\Delta\nu = \frac{1}{2n_g L} \quad (2)$$

where n_g is the group index of the guided mode in the active region. By further assuming $n_g = 3.4$, $\Delta\nu$ ranging from 3 to 32 cm^{-1} are accessible in the experiments.

The design of the outcoupling element, a non-resonant diffraction grating, follows the approach by Jouy and co-workers.^[30] The near-second order grating period is determined by

$$\Lambda = \frac{N - 0.5}{N} \cdot \frac{\lambda}{n_{\text{eff}}} \quad (3)$$

where N is the number of grating periods, n_{eff} the effective guided mode index, and λ the free space wavelength. The outcoupling is investigated with 2D simulations (Lumerical), where the length of the grating section L_{gs} is fixed by $N = 7$ and the fabrication parameters of the respective active region are used (see **Table 1**). The simulation and electric field component responsible for the ver-

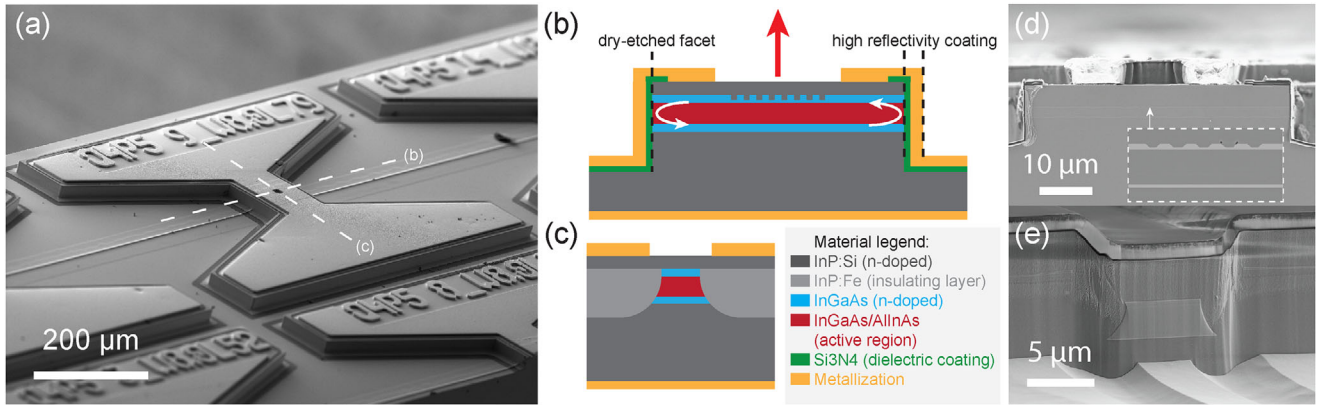


Figure 1. The QCSEL device architecture: a) Scanning electron microscopy (SEM) image of the device after fabrication. The device footprint is below $500 \times 400 \mu\text{m}^2$ and the cavity length is $79 \mu\text{m}$. Light is extracted through the metallic aperture at the center of the device, as indicated by the intersection of the two dashed lines, which represent the axial and lateral directions. The schematic diagrams in (b) and (c) show the axial and the lateral cross-section of the linear cavity, respectively. The red arrow indicates the vertical light extraction. d) SEM image of a cross-section of a $50 \mu\text{m}$ short linear cavity, corresponding to the schematic diagram in (b). The inset displays a magnified view of the grating section where the InGaAs layers are highlighted for clarity. e) SEM image of a dry-etched facet of a test structure showing the etch quality.

tical outcoupling are illustrated in **Figure 3a**. **Figure 3b** considers the transmission toward the surface and the substrate for varying wavelengths, along with the corresponding induced optical losses of a single pass through the grating section. The optical losses are expressed in terms of the length of the grating section L_{gs} using

$$\alpha = -\frac{\ln(1 - T)}{L_{\text{gs}}} \quad (4)$$

where T is the transmission, which corresponds to either the transmission to the surface, the transmission to the substrate, or the transmission back to the input (reflection), though the latter is not shown in **Figure 3b**. For both wavelength ranges, the surface extraction losses α_{surf} are less than 0.1 cm^{-1} , the substrate losses α_{sub} are greater than 0.3 cm^{-1} , and the reflection losses α_{refl} are less than 0.04 cm^{-1} . While for long cavities ($L \gg L_{\text{gs}}$), such an outcoupling element results in small slope efficiencies ($\eta \propto \alpha_{\text{surf}}/\alpha_{\text{tot}}$, where α_{tot} are the total optical losses), an enhancement

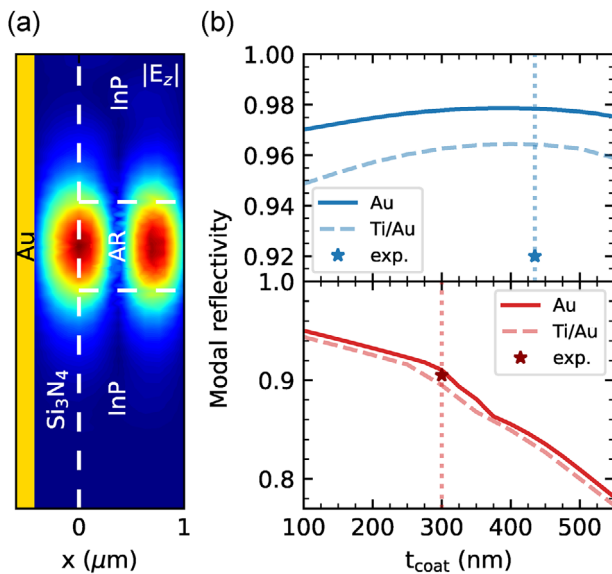


Figure 2. 3D simulation of the facet reflectivity: a) Electric field pattern along the growth direction $|E_z(x, z)|$ for a $1 \mu\text{m}$ long waveguide section terminated with a $\text{Si}_3\text{N}_4/\text{Au}$ coating, assuming a rectangular waveguide with constant width. Here, the wavelength is $4.5 \mu\text{m}$, the active region thickness is $2.03 \mu\text{m}$, and $t_{\text{coat}} = 435 \text{ nm}$. b) Modal reflectivity for varying t_{coat} and wavelengths of $4.5 \mu\text{m}$ (top panel) and $8 \mu\text{m}$ (bottom panel). The dashed lines include a 20 nm thick Ti adhesion layer. The vertical dotted lines correspond to t_{coat} of the fabrication (see **Table 1**) and the stars indicate the experimentally deduced reflectivities discussed below.

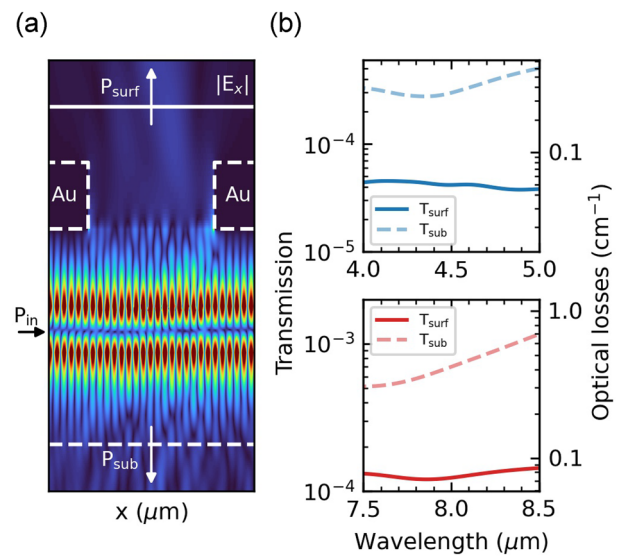


Figure 3. 2D simulation of the outcoupling element using 7 grating periods: a) Electric field pattern along the waveguide $|E_x(x, z)|$ for $\lambda = 8 \mu\text{m}$. The input power P_{in} exciting the axial waveguide mode and the monitors detecting the power directed toward the surface P_{surf} and the substrate P_{sub} are illustrated. b) The transmission T toward the surface $T_{\text{surf}} = P_{\text{surf}}/P_{\text{in}}$ and the substrate $T_{\text{sub}} = P_{\text{sub}}/P_{\text{in}}$ versus the wavelength. The optical losses of a single pass are computed using Equation (4). The grating etch depths and the thicknesses of the top n-InGaAs cladding layers of **Table 1** are used.

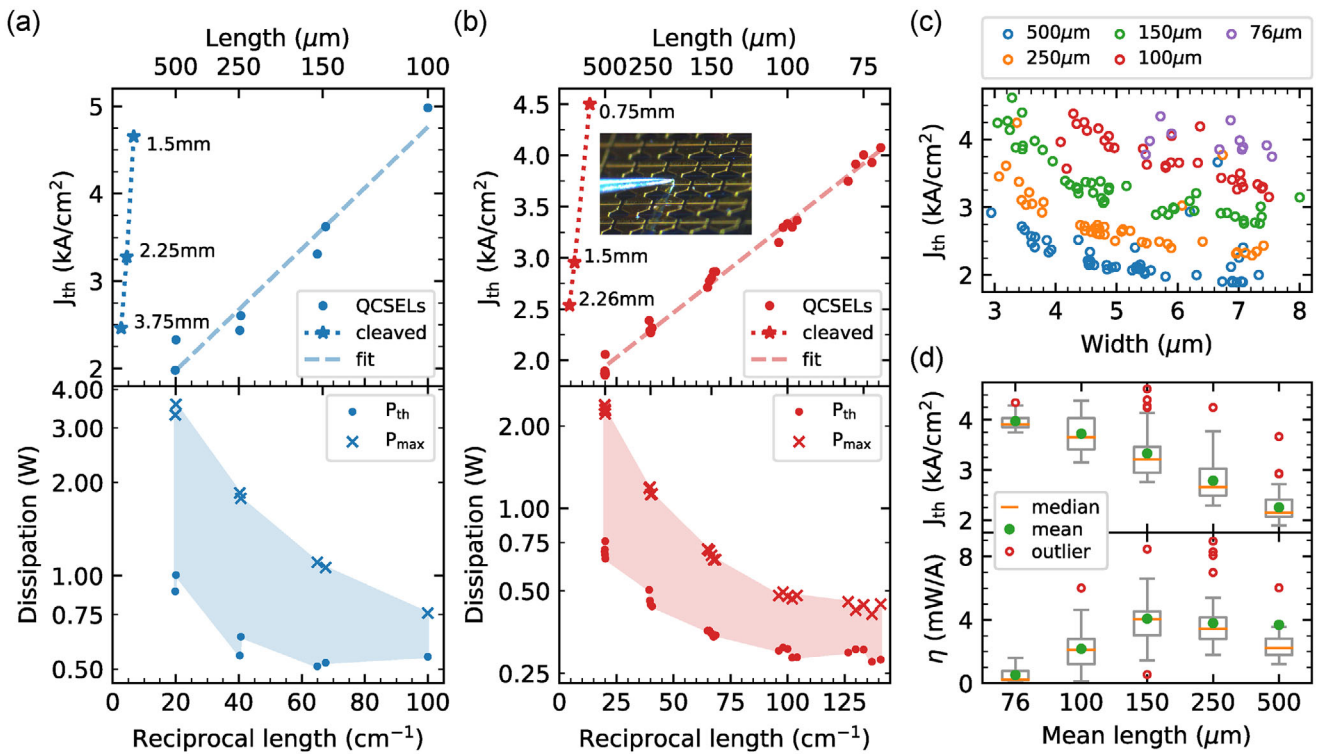


Figure 4. Cavity length scaling for active regions EV1464 (a) and EV2616 (b), with top panels depicting threshold current densities against reciprocal length for both QCSELS and cleaved reference lasers (without extractor), where reference laser lengths are annotated. Bottom panels display the QCSELS' electrical power dissipation in semilogarithmic plots, with device lengths indicated on the top axes. The inset in panel (b) illustrates wafer-level QCSEL probing. Panels (c) and (d) present wafer-level statistics for 171 lasing QCSELS from EV2616: (c) shows threshold current densities versus waveguide width, differentiated by mean device length ($\pm 4 \mu\text{m}$) through color coding, and (d) provides box plots for threshold current densities and slope efficiencies, segmented by mean device length. The boxes span from the first to the third quartile. The whiskers stretch from the box edges to the most distant data point within 1.5 times the interquartile range. Note that the few outliers with $\eta > 10 \text{ mW A}^{-1}$ are not shown to improve data visibility.

of the slope efficiency is expected as the cavity length is scaled ($L \sim L_{\text{gs}}$). This is because the induced surface extraction losses can be seen as localized mirror losses, which are proportional to the reciprocal length. Besides the short grating section, small metallic apertures ($\leq 21.2 \times 10.5 \mu\text{m}^2$) are also used to ensure uniform electrical pumping and sufficient thermal extraction.

To characterize the QCSELS, an automated probe-station was developed to perform light-current-voltage (LIV) characterization on wafer-level, where the individual QCSELS could be addressed with a motorized stage. Light was collected and refocused on the detector using two 3-inch off-axis parabolic mirrors, with the first mirror having a numerical aperture of about 0.7. Either a HgCdTe detector (Vigo systems, model: PVM-2TE-10.6-1x1-TO8-wZnSeAR-70+MIP-DC-250M) or a power meter were used as a detector. For spectral and CW characterization some devices were mounted on submounts. Initially, the QCSELS were characterized in pulsed operation with a repetition rate of 96.15 kHz and a pulse width of 312 ns. Additionally, cleaved reference lasers without any coating and diffraction grating were characterized to estimate the material gain (discussed below) and to determine the average widths of the QCSELS, which are obscured by the HR coatings (see Figure 1). The average widths were computed by fitting the sub-threshold IV curves of the QCSELS to a sub-threshold IV curve of a reference laser with well-known dimensions. Using these widths, instead of individual widths inferred

during the fabrication, more accurate current density values for QCSELS across the whole sample could be obtained. All the measurements presented in the following section were performed at 20°C .

3. Results

To exploit the advantages of short cavity lasers, i.e., single frequency operation at minimal electrical power dissipation on a compact device footprint, high facet reflectivities with values close to unity are required. We estimate these facet reflectivities by measuring the threshold of lasers with varying lengths. The threshold current densities J_{th} of QCSELS and reference lasers are extracted and shown in the top panels of Figure 4a,b. As expected from Equation (1), J_{th} increases linearly with the reciprocal length. The material gain $g\Gamma$ is estimated using Equation (1) and fitting J_{th} of the reference lasers with cleaved facets for which we assume equal reflectivities of 0.28. Finally, with $g\Gamma$, J_{th} of the QCSELS and Equation (1), the reflectivity of the QCSEL facets is deduced. These results are summarized in Table 2 and it can be seen that the experimental reflectivity of 0.905 agrees well with the simulations for EV2616. Albeit a higher experimental reflectivity of 0.92 is obtained for EV1464, the value deviates from the simulated values by more than 0.03. This discrepancy could originate from the roughness induced by dry-etching, which is ne-

Table 2. Reciprocal length study for both active regions: Experimental material gain $g\Gamma$, experimental reflectivity R , and the simulated reflectivity with and without the Ti adhesion layer $\tilde{R}_{\text{Ti}/\text{Au}}$ and \tilde{R}_{Au} , respectively. Note that for the cleaved facets a reflectivity of 0.28 ± 0.01 is assumed.

Active region	$g\Gamma$ [cmkA^{-1}]	R	$\tilde{R}_{\text{Ti}/\text{Au}}$	\tilde{R}_{Au}
EV1464	2.3 ± 0.2	0.92 ± 0.01	0.964	0.978
EV2616	5.7 ± 0.3	0.905 ± 0.005	0.895	0.910

glected in our simulations. Due to the shorter emission wavelength of EV1464 compared to EV2616, we expect the reflectivity of the end-mirrors to be more prone to roughness.

Considering the simulations shown in Figure 2b, the reflectivity at a wavelength of $4.5 \mu\text{m}$ can potentially be improved by more than 0.01. This improvement can be achieved by minimizing the thickness of the Ti adhesion layer, which ultimately reduces the mirror losses by more than 28%. At a wavelength of $8 \mu\text{m}$, the reflectivity can be increased to approximately 0.95 by reducing the coating thickness, with an additional improvement of 0.01 by employing Al_2O_3 as a dielectric coating. This specific improvement is attributed to the lower absorption losses of Al_2O_3 compared to Si_3N_4 , which are generally lower within a range from about 5 to $14 \mu\text{m}$.^[33] It needs to be emphasized that optimizing reflectivity at any given wavelength requires not only minimizing absorption losses but also diffraction losses at the facets. Such optimization depends on the thickness and the complex refractive index of the dielectric coating, as well as the refractive index profile of the waveguide core.

The scaling of the electrical power dissipation versus the reciprocal length is shown in the bottom panels of Figure 4a,b. The filled area illustrates the overall power dissipation, the limiting lower and upper curves indicate the dissipation at threshold P_{th} and at maximum optical power P_{max} , respectively. For a QCSEL based on EV1464 and an active area of $(100 \times 6.8) \mu\text{m}^2$, P_{max} and P_{th} are reduced to 758 and 548 mW, respectively. For a QCSEL based on EV2616 and an active area of $(73 \times 7.1) \mu\text{m}^2$, P_{max} and P_{th} are reduced to 411 and 276 mW, respectively. Among all the characterized QCSELS (>240 lasers), the pulsed LIV characteristics of QCSELS with lowest P_{th} for both active regions are reported in Figure 5. Compared to EV1464 where a P_{th} of 513 mW is observed, a much lower P_{th} of 237 mW could be achieved for EV2616 with the lower sheet doping density. The overall power dissipation can easily be improved by decreasing the doping levels in the claddings and the active region, and by further employing a narrow gain active region.

To evaluate the fabrication process, we consider the characterization of the 2-inch quarter wafer of active region EV2616. On this sample, 242 QCSELS have been characterized and 171 devices reached lasing threshold. The corresponding threshold current densities for the different waveguide widths are presented in Figure 4c. Significant variation in waveguide widths is observed, stemming from both the intentional sweep to minimize the electrically pumped area and the inhomogeneous wet-etching step used to define the waveguide core. By organizing the lasing devices by their mean length ($\pm 4 \mu\text{m}$), the box plots of the threshold current densities and the slope efficiencies are displayed in the top and bottom panel of Figure 4d, respectively.

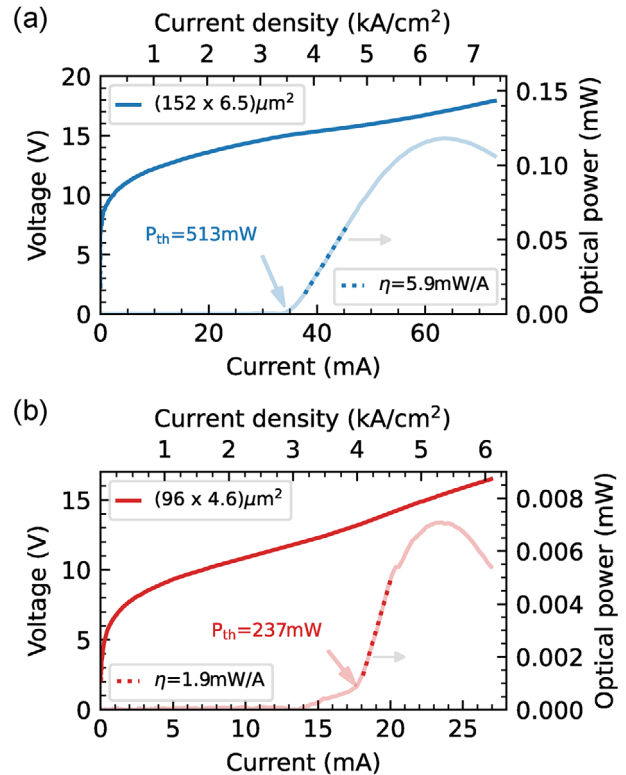


Figure 5. Pulsed light-current-voltage (LIV) characteristics with the lowest power dissipation at threshold P_{th} for QCSELS based on EV1464 (a) and EV2616 (b). The device area and the slope efficiencies η are annotated.

In Figure 6a, we demonstrate the reduction of axial lasing modes toward single-mode operation through cavity length scaling. For QCSELS with varying lengths, the number of modes and the corresponding free spectral range were assessed from spectra acquired for currents close to rollover. The free spectral range is then fitted to Equation (2), resulting in $n_g = 3.30$ and $n_g = 3.44$ for EV1464 and EV2616, respectively. Although still two modes are observed for the shortest device ($L = 71 \mu\text{m}$), this is an encouraging result because the active region is originally designed for broad gain, employing two active region stacks. Moreover, the device lengths are not designed such that the peak of the gain curve is matching an axial cavity mode. Thus, we are convinced that reliable single axial mode selection can be achieved with a narrow gain and single-stack active region featuring a vertical optical transition. Nevertheless, a dominant single mode could be observed with a side mode suppression ratio (SMSR) of 18 dB at 20 mA from a QCSEL based on EV2616 ($L = 104 \mu\text{m}$), as depicted in Figure 6b. This mode is centered at 1347.5 cm^{-1} with the axial mode index $q = 95$ and for larger currents the SMSR decreases as the intensity of the mode $q = 97$ increases. For a QCSEL based on the shorter wavelength active region EV1464 ($L = 152 \mu\text{m}$), the spectra for varying currents are shown in Figure 6c and multiple modes around $4.4 \mu\text{m}$ are observed. Compared to the spectra of the QCSEL shown in Figure 6b, more modes show up due to the longer cavity length and therefore smaller free spectral range. Additionally, from the electroluminescence measurements (see Table 1) we estimate a larger gain bandwidth for the active region

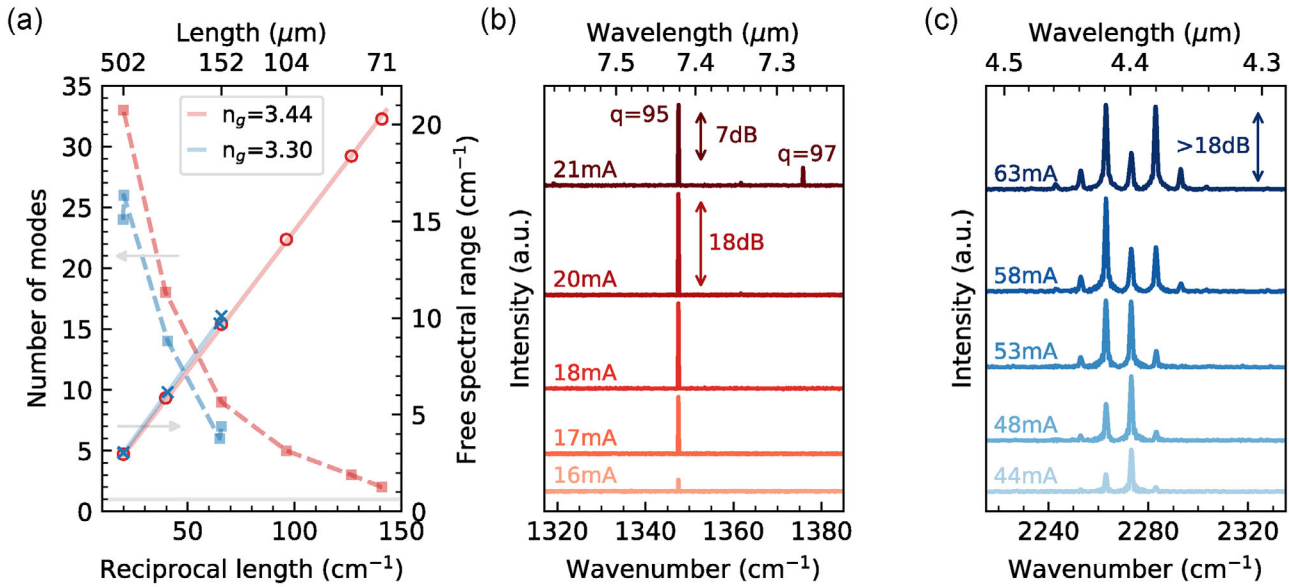


Figure 6. Pulsed spectral characterization of the QCSELS: a) Number of modes (square markers) and free spectral ranges (circle and cross markers) extracted from spectra acquired for currents close to rollover. The solid lines correspond to the fit of the free spectral range (see Equation (2)). The horizontal gray line indicates the number of modes equals one. b) Spectra acquired from a QCSEL with $L = 104 \mu\text{m}$. The axial mode index q and the side mode suppression ratio are illustrated. c) Spectra acquired from a QCSEL with $L = 152 \mu\text{m}$ (corresponding LIV shown in Figure 5a). The arrow indicates the signal-to-noise ratio. Note that all curves appearing blueish are acquired from QCSELS based on EV1464 (wafer-level) with 0.5 cm^{-1} resolution and a pulse width of 52 ns. All curves appearing reddish are acquired from QCSELS based on EV2616 (chip mounted on submounts) with 0.075 cm^{-1} and a pulse width of 52 ns.

EV1464. Single mode emission can be observed when operating the QCSELS in CW. The spectra and the corresponding LIV for a QCSEL based on EV2616 ($L = 248 \mu\text{m}$) is shown in Figure 7. Although the mode selection is not guaranteed, only one mode appears and at 45 mA a SMSR larger than 33 dB is deduced. It needs to be emphasized, that the chip used for these CW measurements is mounted on a submount with epitaxial layer up and that improvements are expected from a thinner substrate or from a double-channel geometry.^[27]

An enhancement of the slope efficiency, as discussed above, is demonstrated in Figure 8a, showing that for $L \geq 146 \mu\text{m}$, the slope efficiency increases roughly linearly with the reciprocal length, as expected. For smaller values of L , the slope efficiency then drops because J_{th} increases close to the maximum current density J_{max} , which can be seen from the corresponding LIV characteristics shown in Figure 8b. To extend the enhancement of the slope efficiency for shorter cavities, higher reflectivities of the end-mirrors are required.

In Figure 8c,d, the pulsed LIV characteristics and the wall-plug efficiencies of QCSELS exhibiting the largest slope efficiencies are reported. The values for the slope efficiencies are 44.4 and 75.7 mW A^{-1} for EV1464 and EV2616, respectively. These exceptionally higher values might be explained by a more favorable alignment between the dry-etched end-mirrors or by unintentional air voids during the regrowth step after wet-etching the grating. Instead, creating air voids on purpose by a two-step regrowth, employing a thicker etch step into the n-InGaAs cladding layer, or extending the area of the metallic aperture, provide ways to increase the surface extraction losses and thus to enhance the slope efficiency.

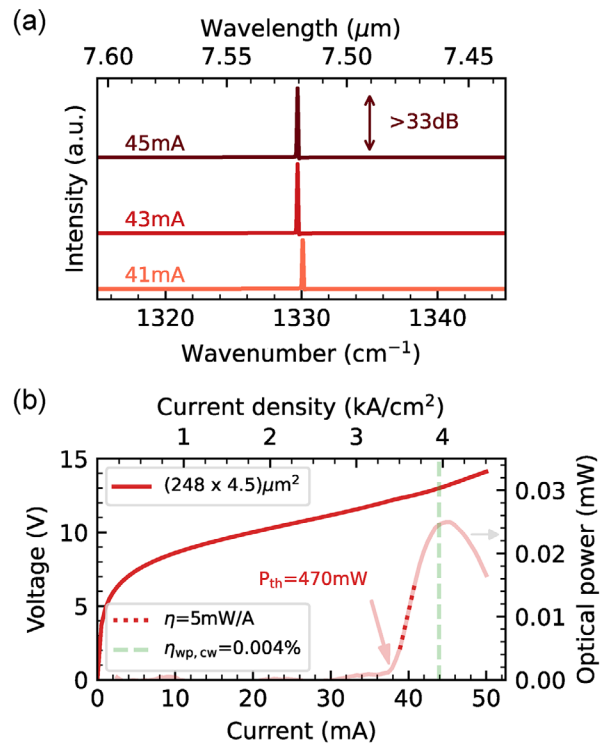


Figure 7. Continuous wave characterization of a QCSEL based on a chip of EV2616, which was mounted on a submount: a) Spectra acquired with a resolution of 0.075 cm^{-1} . The side mode suppression ratio is illustrated for a current of 45 mA. b) LIV characteristics including annotations for device area, slope efficiency η , maximum wall-plug efficiency $\eta_{\text{wp,cw}}$, and threshold dissipation power P_{th} .

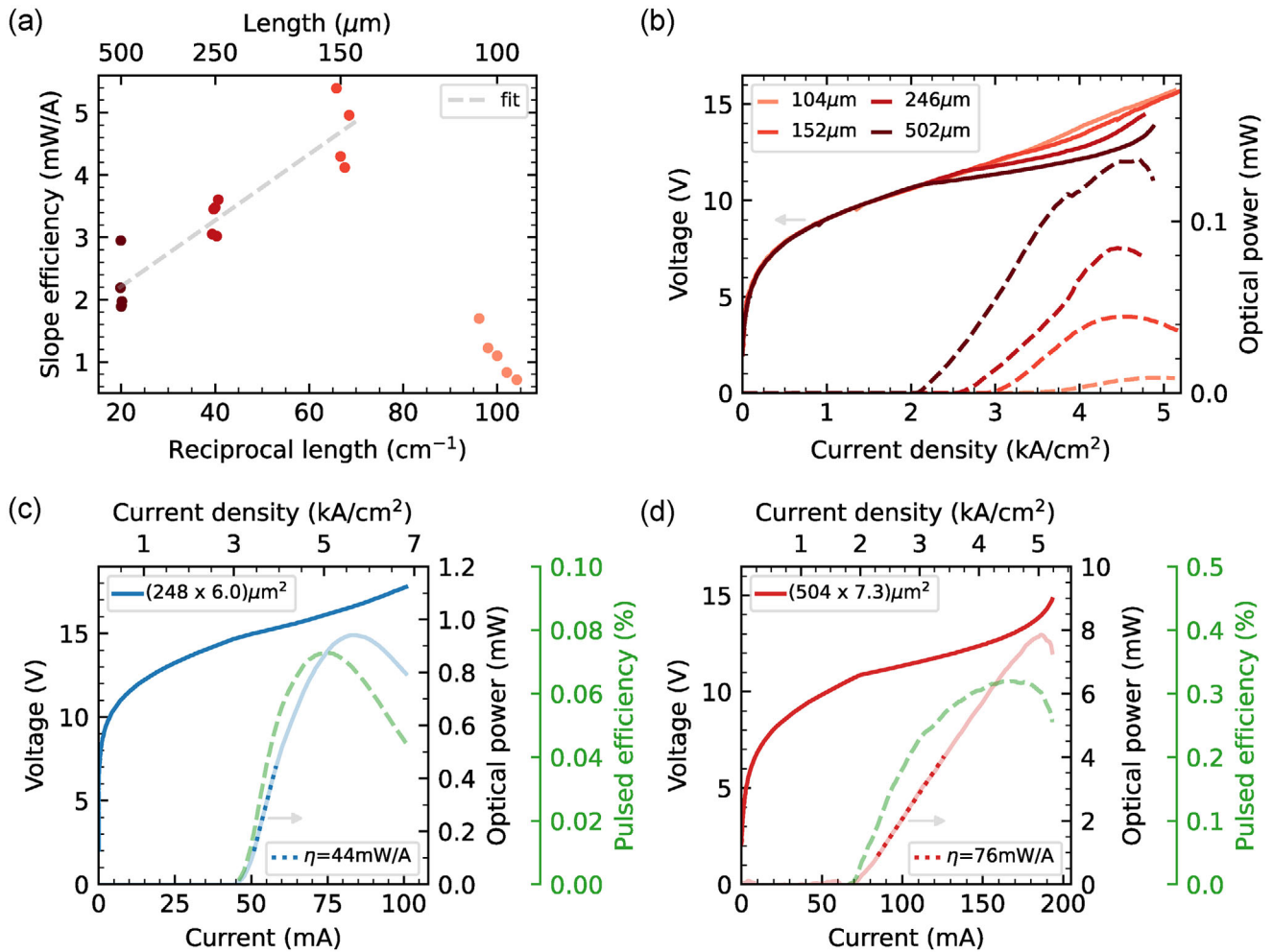


Figure 8. a) Slope efficiency versus the reciprocal length extracted from LI curves of QCSELS based on EV2616 with widths within $(4.8 \pm 0.2) \mu\text{m}$. b) Pulsed LIV characteristics for a selection of QCSELS used in (a). The device lengths are annotated. For panels (c) and (d), pulsed LIV characteristics exhibiting the largest slope efficiencies for QCSELS based on EV1464 (c) and EV2616 (d). The green dashed curves show the pulsed wall-plug efficiencies over the current. The device areas and the slope efficiencies η are annotated.

Because wall-plug efficiency linearly scales with slope efficiency, optimizing the outcoupling element for larger surface extraction losses is critical for improving wall-plug efficiency, which is currently limited to below 0.032 % (see Figure 8d). Lastly, further improvement of the wall-plug efficiency is anticipated by optimizing the internal quantum efficiency of dedicated narrow gain active regions.

4. Conclusion

We have proposed the QCSEL for the next generation of portable and large scale applications relying on gas phase absorption spectroscopy. The QCSEL was implemented as a compact buried heterostructure laser with footprints well below $(500 \times 400) \mu\text{m}^2$ based on two different active regions designed for 4.5 and 8 μm. Lasing is demonstrated for devices as short as 71 μm, showing that higher integration densities are feasible. The key to further scaling down the cavity length, while also reducing the electrical power dissipation and the number of axial lasing modes, is to increase the mirror reflectivities above the 0.92 achieved in

this work. This can be done by leveraging on high-quality dry-etching, minimizing the Ti adhesion layer, and adjusting the dielectric coating and the refractive index profile of the waveguide core. To reduce the power dissipation below 237 mW and to guarantee single axial mode selection, low-doped and narrow-gain active regions will be combined with cavity lengths designed such that a single axial mode is matching the peak wavelength of the gain curve.

Acknowledgements

The authors gratefully acknowledge the financial support from Innosuisse - Swiss Innovation Agency (Innovation Projects: 52899.1 and 53098.1) and the ETH Zürich Foundation (Project: 2020-HS-348). The authors express their gratitude to Zhixin Wang and Ruijun Wang for useful discussions and conceiving ideas. Furthermore, the authors would like to thank Bo Meng for helpful hints on device fabrication, Moritz Müller for developing further the automated probe-station, and Philipp Täschler for valuable inputs on the manuscript text.

Open access funding provided by Eidgenössische Technische Hochschule Zurich.

Conflict of Interest

The authors declare no conflict of interest.

Data Availability Statement

The data that support the findings of this study are available from the corresponding author upon reasonable request.

Keywords

high volume fabrication, low dissipation, mid-infrared, quantum cascade lasers, single mode, surface emission, wafer-level testing

Received: July 18, 2023

Revised: February 16, 2024

Published online: April 8, 2024

- [1] P. F. Bernath, *Spectra of Atoms and Molecules*, 4 edition, Oxford University Press, New York **2020**.
- [2] I. E. Gordon, L. S. Rothman, C. Hill, R. V. Kochanov, Y. Tan, P. F. Bernath, M. Birk, V. Boudon, A. Campargue, K. V. Chance, B. J. Drouin, J. M. Flaud, R. R. Gamache, J. T. Hodges, D. Jacquemart, V. I. Perevalov, A. Perrin, K. P. Shine, M. A. Smith, J. Tennyson, G. C. Toon, H. Tran, V. G. Tyuterev, A. Barbe, A. G. Császár, V. M. Devi, T. Furtenbacher, J. J. Harrison, J. M. Hartmann, A. Jolly, et al., *J. Quant. Spectrosc. Radiat. Transfer* **2017**, *203*, 3.
- [3] J. Hodgkinson, R. P. Tatam, *Meas. Sci. Technol.* **2012**, *24*, 012004.
- [4] D. Popa, F. Udrea, *Sensors* **2019**, *19*, 2076.
- [5] M. Serena Vitiello, G. Scalari, B. Williams, P. De Natale, J. Faist, F. Capasso, D. L. Sivco, C. Sirtori, A. L. Hutchinson, A. Y. Cho, *Opt. Express* **2015**, *23*, 5167.
- [6] B. Hinkov, A. Hugi, M. Beck, J. Faist, *Opt. Express* **2016**, *24*, 3294.
- [7] B. Argence, B. Chanteau, O. Lopez, D. Nicolodi, M. Abgrall, C. Chardonnet, C. Daussy, B. Darquié, Y. Le Coq, A. Amy-Klein, *Nat. Photonics* **2015**, *9*, 456.
- [8] F.-L. Yan, J.-C. Zhang, D.-Y. Yao, F.-Q. Liu, L.-J. Wang, J.-Q. Liu, Z.-G. Wang, *Chin. Phys. B* **2015**, *24*, 024212.
- [9] (Ed.: R. Michalzik), *VCSELS*, vol. 166, Springer, Berlin, Heidelberg **2013**.
- [10] W. W. Bewley, C. L. Canedy, C. S. Kim, C. D. Merritt, M. V. Warren, I. Vurgaftman, J. R. Meyer, M. Kim, *Appl. Phys. Lett.* **2016**, *109*, 151108.
- [11] G. K. Veerabathran, S. Sprengel, A. Andrejew, M. C. Amann, *Appl. Phys. Lett.* **2017**, *110*, 7.
- [12] V. Jayaraman, B. Kolasa, C. Lindblad, A. Cazabat, C. Burgner, S. Segal, K. Lascola, F. Towner, F. Xie, in *Vertical-Cavity Surface-Emitting Lasers* XXIV (Eds.: L. A. Graham, C. Lei), International Society for Optics and Photonics, vol. 11300, SPIE, Bellingham, WA **2020**, p. 113000M.
- [13] J. Faist, *Quantum Cascade Lasers*, Oxford University Press, New York **2013**.
- [14] E. Mujagić, L. K. Hoffmann, S. Schartner, M. Nobile, W. Schrenk, M. P. Semtsiv, M. Wienold, W. T. Masselink, G. Strasser, *Appl. Phys. Lett.* **2008**, *93*, 161101.
- [15] E. Mujagić, M. Nobile, H. Detz, W. Schrenk, J. Chen, C. Gmachl, G. Strasser, *Appl. Phys. Lett.* **2010**, *96*, 031111.
- [16] E. Mujagić, C. Schwarzer, Y. Yao, J. Chen, C. Gmachl, G. Strasser, *Appl. Phys. Lett.* **2011**, *98*, 141101.
- [17] C. Schwarzer, E. Mujagić, S. I. Ahn, A. M. Andrews, W. Schrenk, W. Charles, C. Gmachl, G. Strasser, *Appl. Phys. Lett.* **2012**, *100*, 191103.
- [18] R. Szedlak, C. Schwarzer, T. Zederbauer, H. Detz, A. Maxwell Andrews, W. Schrenk, G. Strasser, *Opt. Express* **2014**, *22*, 15829.
- [19] J. Faist, C. Gmachl, M. Striccoli, C. Sirtori, F. Capasso, D. L. Sivco, A. Y. Cho, *Appl. Phys. Lett.* **1996**, *69*, 2456.
- [20] C. Gmachl, J. Faist, F. Capasso, C. Sirtori, D. L. Sivco, A. Y. Cho, *IEEE J. Quantum Electron.* **1997**, *33*, 1567.
- [21] S. Höfling, J. Reithmaier, A. Forchel, *IEEE J. Sel. Top. Quantum Electron.* **2005**, *11*, 1048.
- [22] R. A. Cendejas, Z. Liu, W. Sánchez-Vaynshteyn, C. G. Caneau, C. Zah, C. Gmachl, *IEEE Photonics J.* **2011**, *3*, 71.
- [23] A. Wittmann, Y. Bonetti, M. Fischer, J. Faist, S. Blaser, E. Gini, *IEEE Photonics Technol. Lett.* **2009**, *21*, 814.
- [24] A. Bismuto, S. Blaser, R. Terazzi, T. Gresch, A. Müller, J. Faist, F. Capasso, D. L. Sivco, C. Sirtori, A. L. Hutchinson, A. Y. Cho, *Opt. Express* **2015**, *23*, 5477.
- [25] F. Wang, S. Slivken, D. H. Wu, M. Razeghi, *Opt. Express* **2020**, *28*, 17532.
- [26] Y. Bai, N. Bandyopadhyay, S. Tsao, S. Slivken, M. Razeghi, *Appl. Phys. Lett.* **2011**, *98*, 181102.
- [27] F. Cheng, J. Zhang, Y. Guan, P. Yang, N. Zhuo, S. Zhai, J. Liu, L. Wang, S. Liu, F. Liu, Z. Wang, *Opt. Express* **2020**, *28*, 36497.
- [28] Z. Wang, F. Kapsalidis, R. Wang, M. Beck, J. Faist, *Nat. Commun.* **2022**, *13*, 1.
- [29] D. Y. Yao, J. C. Zhang, F. Q. Liu, N. Zhuo, F. L. Yan, L. J. Wang, J. Q. Liu, Z. G. Wang, *Appl. Phys. Lett.* **2013**, *103*, 041121.
- [30] P. Jouy, C. Bonzon, J. Wolf, E. Gini, M. Beck, J. Faist, *Appl. Phys. Lett.* **2015**, *106*, 071104.
- [31] M. Beck, D. Hofstetter, T. Aellen, J. Faist, U. Oesterle, M. Illegems, E. Gini, H. Melchior, *Science* **2002**, *295*, 301.
- [32] M. J. Süess, R. Peretti, Y. Liang, J. M. Wolf, C. Bonzon, B. Hinkov, S. Nida, P. Jouy, W. Metaferia, S. Lourdudoss, M. Beck, J. Faist, *Photonics* **2016**, *3*, 26.
- [33] J. Kischkat, S. Peters, B. Gruska, M. Semtsiv, M. Chashnikova, M. Klinkmüller, O. Fedosenko, S. Machulik, A. Aleksandrova, G. Monastyrskiy, Y. Flores, W. T. Masselink, *Appl. Opt.* **2012**, *51*, 6789.